BMC Medical Imaging

RESEARCH

Open Access

Analysis of MRI imaging characteristics in 10 cases of adult granulosa cell tumor with normal estrogen levels

Wei Weng[1], Yaomeng Chen[1], Ze Liu[2], Weiqian Chen[3], Jiejie Hu[4], Huihui Chen[4], Xindian Pan[4], Hai Wu[1] and Xinle Chi[1*]

Abstract

Objective This study investigates the MRI characteristics of primary and metastatic adult granulosa cell tumor with normal estrogen levels (AGCT-NEL) to enhance clinical understanding and diagnostic accuracy of this disease.

Methods We collected clinical data from 10 patients with AGCT-NEL, confirmed by pathology, treated at our hospital from January 2016 to January 2024. We retrospectively analyzed the MRI features of primary and metastatic lesions from aspects such as shape, edge characteristics, MRI signal, and enhancement features.

Results A total of 10 AGCT-NEL patients were included in this study, aged 28 to 81 years, with an average age of 54 ± 16 years. The primary tumors primarily presented as unilocular cystic, solid, and cystic-solid types. The solid components showed isointense to slightly hypointense signals on T1-weighted imaging (T_1WI), slightly hyperintense signals on T2-weighted imaging (T_2WI), and high signals on diffusion-weighted imaging (DWI), with possible internal hemorrhage or cystic degeneration. The cystic components exhibited low signal on T_1WI, high signal on T_2WI, uniform wall thickness, and no wall nodules, typically showing hemorrhagic fluid levels. Honeycomb and Swiss cheese signs are sometimes observed in cystic-solid tumors. All metastatic lesions were cystic (either unilocular or multilocular), presenting low signal on T_1WI and high signal on T_2WI, with no wall nodules and possible internal hemorrhagic fluid levels. The multilocular metastatic tumors demonstrated unevenly thickened partitions, also displaying honeycomb and Swiss cheese signs.

Conclusion The MRI characteristics of primary and metastatic lesions in AGCT-NEL possess specific features, such as signs of hemorrhage, absence of wall nodules in the cystic portions of the tumors, and distinctive honeycomb and Swiss cheese signs, with metastatic lesions being cystic. Understanding these features can aid in improving preoperative diagnostic capabilities and reducing misdiagnosis.

Keywords Reproductive system, Oncology, Ovaries, Adult ovarian granulosa cell tumor, Magnetic resonance imaging

*Correspondence:
Xinle Chi
1740986267@qq.com
[1]Department of Radiology, The Wenzhou Third Clinical Institute Affiliated to Wenzhou Medical University, Wenzhou People's Hospital, Wenzhou, Zhejiang 325000, China
[2]Department of Radiology, Ningbo Ninth Hospital, Ningbo, Zhejiang 315000, China
[3]Department of Respiratory Medicine, The Wenzhou Third Clinical Institute Affiliated to Wenzhou Medical University, Wenzhou People's Hospital, Wenzhou, Zhejiang 325000, China
[4]Department of Pathology, The Wenzhou Third Clinical Institute Affiliated to Wenzhou Medical University, Wenzhou People's Hospital, Wenzhou, Zhejiang 325000, China

Background

Ovarian granulosa cell tumor (OGCT) is classified as a sex cord-stromal tumor of the ovary, originating from developing gonadal stromal cells. This tumor is relatively rare, classified as low-grade malignant, with a small percentage showing distant metastasis and a tendency for postoperative recurrence [1–3]. OGCT can be divided into two types: adult granulosa cell tumor (AGCT) and juvenile granulosa cell tumor, with AGCT accounting for 95% of cases. AGCT can occur at any age but is most commonly found in perimenopausal or postmenopausal women, and can also affect women in their reproductive years or prepubescent girls [4]. OGCT typically exhibits estrogen-secreting functionality, with abnormal estrogen levels leading to characteristic complications that can aid in clinical diagnosis. However, approximately 30% of OGCT cases are atypical, presenting with normal estrogen levels [5], making differentiation from other tumor types or ovarian tumors challenging and often resulting in misdiagnosis. Given that AGCT is the primary subtype of OGCT, it is crucial to enhance the understanding of imaging characteristics of AGCT with normal estrogen levels (AGCT-NEL). MRI is the primary imaging modality for diagnosing reproductive system tumors, playing an irreplaceable role in the localization, characterization, and staging of ovarian tumors. However, there is currently insufficient reporting on the MRI imaging characteristics of AGCT-NEL. Therefore, this study aims to retrospectively analyze the MRI findings and relevant clinical and pathological features of AGCT-NEL, with the goal of improving clinical sensitivity and diagnostic capability regarding this condition.

Patients and methods

Study population and baseline data

This study has received approval from the hospital's ethics committee. Inclusion criteria for patients were: (1) diagnosis of AGCT confirmed by postoperative pathology between January 2016 and January 2024 at our hospital; (2) normal estrogen levels in patients; (3) availability of MRI examination records. Exclusion criteria included: (1) juvenile granulosa cell tumor; (2) significant artifacts present in MRI images. Baseline data collected included patients' age, menopausal status, tumor marker levels, clinical symptoms, pathological results, and postoperative prognosis.

MRI equipment and imaging protocols

Imaging was performed using a Siemens Tim 1.5T superconducting MRI scanner. A body phased array coil was utilized, and the scanning range extended from the anterior superior iliac spine to the superior margin of the pubic symphysis. A turbo spin echo (TSE) sequence was employed for imaging, with the following scan parameters: axial view: TSE T1-weighted imaging (T_1WI) (TR 450 ms, TE 11 ms, slice thickness 9 mm), TSE T2-weighted imaging (T_2WI) (TR 3800 ms, TE 99 ms, slice thickness 9 mm), and T_2WI with fat suppression (TR 5870 ms, TE 85 ms, TI 150 ms, slice thickness 9 mm). Sagittal view: TSE T_2WI (TR 3300 ms, TE 104 ms, slice thickness 6 mm). Coronal view: TSE T_2WI (TR 5500 ms, TE 94 ms, slice thickness 5 mm). The number of signal averages (NSA) was 2–3, with a matrix size of 512×512. Diffusion-weighted imaging (DWI) used a single-shot echo planar imaging (SSEPI) sequence, with a b-value of 800 s/mm². For contrast-enhanced scans, gadopentetate dimeglumine (Gd-DTPA) was injected via the antecubital vein under high pressure, at a dose of 0.25 mmol/kg and an injection rate of 2.5 ml/s. The volumetric interpolated breath-hold examination (VIBE) was used for axial, coronal, and sagittal T_1WI scans. Scan parameters were: TR 4.9 ms, TE 2.4 ms, slice thickness 3 mm. Scans were performed at 30 s, 60 s, and 180 s post-contrast injection, with a 20-second delay between each phase, capturing images during the arterial, venous, and delayed phases.

MRI features analysis

MRI images were independently analyzed by a senior attending radiologist and a radiology department head. The MRI signal of the mass was referenced to the myometrium. The analysis included the location, number, size, shape, edge characteristics, mode of metastasis, FIGO staging, apparent diffusion coefficient (ADC) values of the solid portions, and features of both plain and enhanced imaging. Additionally, the signal intensity of the solid portion of the mass was compared with that of the myometrium during T_1WI, T_2WI, and during the arterial phase of enhancement.

Pathological results analysis

A senior pathologist conducted a retrospective summary of the pathological results of the enrolled patients, including the macroscopic and microscopic observations of the masses, as well as the immunohistochemical results.

Statistical analysis

Statistical analysis was performed using SPSS version 25.0. The Kappa test was employed to evaluate the consistency of the observations between the two radiologists. A Kappa value ≥ 0.75 indicated good consistency, a Kappa value between 0.40 and 0.75 indicated moderate consistency, and a Kappa value < 0.40 indicated poor consistency. Differences were considered statistically significant at $P<0.05$.

Results

Baseline data of patients

A total of 10 patients with AGCT-NEL were enrolled in this study, with baseline data shown in Table 1. The age of the 10 patients ranged from 28 to 81 years, with an average age of 54±16 years. Among them, 6 patients were postmenopausal. One patient had an elevated CA-125 level of 76.4 U/ml (normal value < 35 U/ml), while the tumor markers for the remaining patients were normal. Among the 10 patients, 3 presented with irregular vaginal bleeding, 1 with lower abdominal pain, and the others had no significant symptoms. Pathological results indicated that among the 10 patients, 3 had simple endometrial hyperplasia, 1 had complex endometrial hyperplasia, 1 had a uterine leiomyoma, and 2 had adenomyosis. In the follow-up after surgery, 8 patients had no recurrence, 1 patient was lost to follow-up, and 1 patient experienced a recurrence 2 years post-operation.

MRI features of AGCT-NEL

Primary tumors

Among the 10 patients, 9 had primary tumors, and 2 had metastatic tumors. The basic characteristics of all tumors are presented in Table 2. A total of 9 primary tumors were identified in 9 patients, with 6 located in the right adnexa and 3 in the left adnexa. The maximum diameter of the tumors ranged from 2.9 cm to 21.4 cm (average 8.1 cm), with the FIGO staging primarily being IA or IC [6].

Unilocular cystic tumor (patient 9, Fig. 1) The tumor was round with clear borders; the cystic portion exhibited low signal on T_1WI and very high signal on T_2WI. On DWI, it showed slightly higher signal intensity, with an ADC value of 2.940×10^{-3} mm²/s. A hemorrhagic fluid level was visible within the tumor, and there was significant enhancement of the cyst wall after contrast administration, with no enhancement within the cyst.

Solid tumors (patients 1, 3, 7) Three solid tumors were found, presenting as oval or round shapes with clear margins. All tumors exhibited homogeneous signals, appearing as isointense or slightly hypointense on T_1WI and slightly hyperintense on T_2WI. DWI showed high signal intensity, and ADC values ranged from 0.520 to 0.913 ($\times10^{-3}$ mm²/s), with significant enhancement observed after contrast enhancement. Two of the tumors exhibited high signal on T_1WI, indicating hemorrhage, and both displayed patchy high signals on T_2WI. The MRI findings for Patient 7 are shown in Fig. 2. The signal intensity ratios of the tumors compared to the myometrium during T_1WI, T_2WI, and arterial phase enhancement were 1.019 to 1.340, 1.186 to 1.500, and 0.800, respectively (Table 2).

Cystic-solid tumors (patients 2, 4, 5, 6, 8) In this group, there were five cystic-solid tumors: three were oval-shaped and two exhibited irregular shapes. The lesions had clear boundaries, with varying-sized cystic areas demonstrating low signal intensity on T_1WI and very high signal intensity on T_2WI. The distribution was locally clustered, presenting honeycomb and Swiss cheese signs. The solid portions showed isointense to slightly hypointense signal on T_1WI and slightly hyperintense signal on T_2WI, with ADC values ranging from 0.630 to 0.783 ($\times10^{-3}$ mm²/s). Among the five tumors, three exhibited patchy or irregular high signal intensity on T_1WI, indicative of hemorrhage. After contrast enhancement, there was significant enhancement of the cyst wall and the solid portion, while no enhancement was observed within the cyst. The MRI findings for Patient 2 are illustrated in Fig. 3. In the solid components, the signal intensity ratios compared to the myometrium during T_1WI, T_2WI, and arterial phase enhancement were 0.980 to 1.171, 1.131 to 1.312, and 0.720 to 0.920, respectively (Table 2).

Table 1 Baseline data

Patient Number	Age	Whether menopause	Tumor Marker Levels	Symptoms	Other Pathological Changes	Postoperative Prognosis
1	41	No	Normal		Simple Endometrial Hyperplasia	No recurrence in 10.4 years
2	52	Yes	Normal		Uterine Adenomyosis; Simple Endometrial Hyperplasia	No recurrence in 9.8 years
3	66	Yes	CA125: 76.4U/ml(↑)	Irregular Vaginal Bleeding	Uterine Leiomyoma; Complex Endometrial Hyperplasia	No recurrence in 10.4 years
4	81	Yes	Normal	Irregular Vaginal Bleeding		No recurrence in 9.3 years
5	66	Yes	Normal			loss to follow-up
6	42	No	Normal	Irregular Vaginal Bleeding; lower Abdominal Pain		No recurrence in 2.8 years
7	28	No	Normal		Uterine Adenomyosis	No recurrence in 2.3 years
8	58	Yes	Normal			No recurrence in 2.3 years
9	72	Yes	Normal		Simple Endometrial Hyperplasia	No recurrence in 10.3 years
10	38	No	Normal			Recurrence after 2.0 years

Table 2 MRI features of primary and metastatic lesions

Patient Number	Number of Lesions	Primary Tumor	Metastatic Tumor	Metastatic Route	Location	Maximum Diameter	FIGO Staging	Shape	Edge	DWI(b=800 s/mm^2)	ADC ($\times 10^{-3}$ mm^2/s)	MRI Imaging Findings	MRI Enhanced Findings	Tumor-to-muscle on T1WI(Solid Portion)	Tumor-to-muscle on T2WI(Solid Portion)	Tumor-to-muscle on enhanced T1WI(Solid Portion)
1	1	1	0		Left Adnexa	4.0 cm	IA	Oval; Solid	well-defined	High	Solid: 0.520	There are three main types of masses: unilocular cystic, solid, and cystic-solid. The solid portion appears isointense to slightly hypointense on T1WI, slightly hyperintense on T2WI, and shows high signal intensity on DWI, with the potential presence of hemorrhage or cystic degeneration. The cystic portion has a uniformly thick wall with no nodules, typically displaying a hemorrhagic fluid level. Honeycomb and Swiss cheese signs are distinctive features of cystic-solid masses.		1.019	1.186	
2	1	1	0		Left Adnexa	6.3 cm	IA	Round; cystic-solid	well-defined	High	Solid: 0.663; Cystic Portion Too Small to Measure		Solid Portion Exhibits Marked Enhancement	1.171	1.208	0.720
3	1	1	0		Right Adnexa	2.9 cm	IA	Round; Solid	well-defined	High	Solid: 0.913			1.020	1.267	
4	1	1	0		Right Adnexa	6.0 cm	IC	Round; Cystic-Solid, Predominantly Cystic	well-defined	High, Slightly High	Solid: 0.783; Cystic: 2.567			1.153	1.256	
5	1	1	0		Right Adnexa	7.0 cm	IA	Round; cystic-solid	well-defined	Slightly High	Solid: 0.690; Cystic: 2.785		Solid Portion and Cyst Wall Exhibit Marked Enhancement	1.08	1.23	0.920
6	1	1	0		Right Adnexa	12.7 cm	IA	irregular; cystic-solid	well-defined	Slightly High	Solid: 0.630; Cystic: 2.880			1.123	1.312	
7	1	1	0		Left Adnexa	3.5 cm	IC	Round; Solid	well-defined	High	Solid: 0.656		Marked Enhancement	1.340	1.500	0.800
8	1	1	0		Right Adnexa	21.4 cm	IC	irregular; cystic-solid	well-defined	Mixed High	Solid: 0.754; Cystic: 2.678			0.98	1.131	
9	11	1		dissemination, distant metastasis	Right Adnexa	8.8 cm	IIIC	Round; unilocular cystic	well-defined	Slightly High	Cystic: 2.940		Cyst Wall Exhibits Marked Enhancement, with No Enhancement Inside the Cyst			

Table 2 (continued)

Patient Number	Number of Lesions	Primary Tumor	Metastatic Tumor	Metastatic Route	Location	Maximum Diameter	FIGO Staging	Shape	Edge	DWI(b=800 s/mm²)	ADC ($\times10^{-3}$ mm²/s)	MRI Imaging Findings	MRI Enhanced Findings	Tumor-to-muscle on T1WI(Solid Portion)	Tumor-to-muscle on T2WI(Solid Portion)	Tumor-to-muscle on enhanced T1WI(Solid Portion)
			10		mesoappendix, mesentery, sigmoid colon, and peri-uterine tissue	3.0 cm		Round; multilocular cystic	well-defined	High, Slightly High	unilocular cystic: 2.920; multilocular cystic: 2.780	The metastatic lesions are all cystic, appearing hypointense on T1WI and hyperintense on T2WI, with no wall nodules; they may contain hemorrhagic fluid levels. Multilocular cystic metastatic tumors exhibit unevenly thick septations, with honeycomb and Swiss cheese signs visible.	Cyst Wall Exhibits Marked Enhancement, with No Enhancement Inside the Cyst			
10	1	0	1		rectal fossa	2.5 cm	IIIA	Round; multilocular cystic	well-defined	High						

Metastatic tumors

Among the two patients with metastases, there were a total of 11 masses. In one case, there was a primary tumor in the right adnexa with multiple pelvic metastases, totaling 10 metastatic masses which displayed both implantative and distant metastasis, involving the mesoappendix, mesentery, sigmoid colon, and peri-uterine tissue, with the largest diameter approximately 3.0 cm. This case was classified as FIGO stage IIIC (Patient 9). The other case involved a single mass which represented a solitary distant metastasis in the rectal area after surgery (no primary lesion was present), with a diameter of about 2.5 cm, classified as FIGO stage IIIA (Patient 10).

Unilocular cystic tumors (3 tumors from patient 9, Fig. 4) The metastatic lesions were round in shape with clear borders, showing low signal on T_1WI, high signal on T_2WI, and slightly higher signal on DWI, with an average ADC value of 2.920 ($\times10^{-3}$ mm²/s). One of the tumors exhibited hemorrhage, demonstrating a hemorrhagic fluid level. After enhancement, there was significant enhancement of the cyst wall, while no enhancement was observed within the cyst.

Multilocular cystic tumors (8 tumors, 7 in patient 9 and 1 in patient 10) The masses are oval-shaped with unevenly thickened septations, and when there are multiple septations, honeycomb and Swiss cheese signs are observable (Fig. 4). The tumors exhibit low signal on T_1WI, high signal on T_2WI, with heterogeneous signals, and slightly higher signal on DWI, with an average ADC value of 2.780 ($\times10^{-3}$ mm²/s). Five of the tumors showed hemorrhage, with a visible hemorrhagic fluid levels. After enhancement, significant enhancement of the cyst walls and septa was observed, while there was no enhancement within the cysts. Patient 10 had fewer septations, and the MRI findings are shown in Fig. 5.

Pathological results

All 10 patients underwent surgical treatment, and the intraoperative findings regarding the location, size, and morphology of the masses were generally consistent with the MRI observations. The gross examination of the specimens revealed that the masses in the 10 patients had varying degrees of softness, with gelatinous areas present within the cystic foci. Under microscopy, the tumor cells appeared predominantly round, oval, or polygonal, with some showing lobulation. The cells were arranged in clusters or strands, with visible nuclear grooves and interspersed fibrous tissue components, along with capillary lumina of varying sizes. All 10 patients exhibited varying numbers of Call-Exner bodies, which showed eosinophilic proteinaceous material and discernible condensed nuclei. Eight patients underwent immunohistochemical

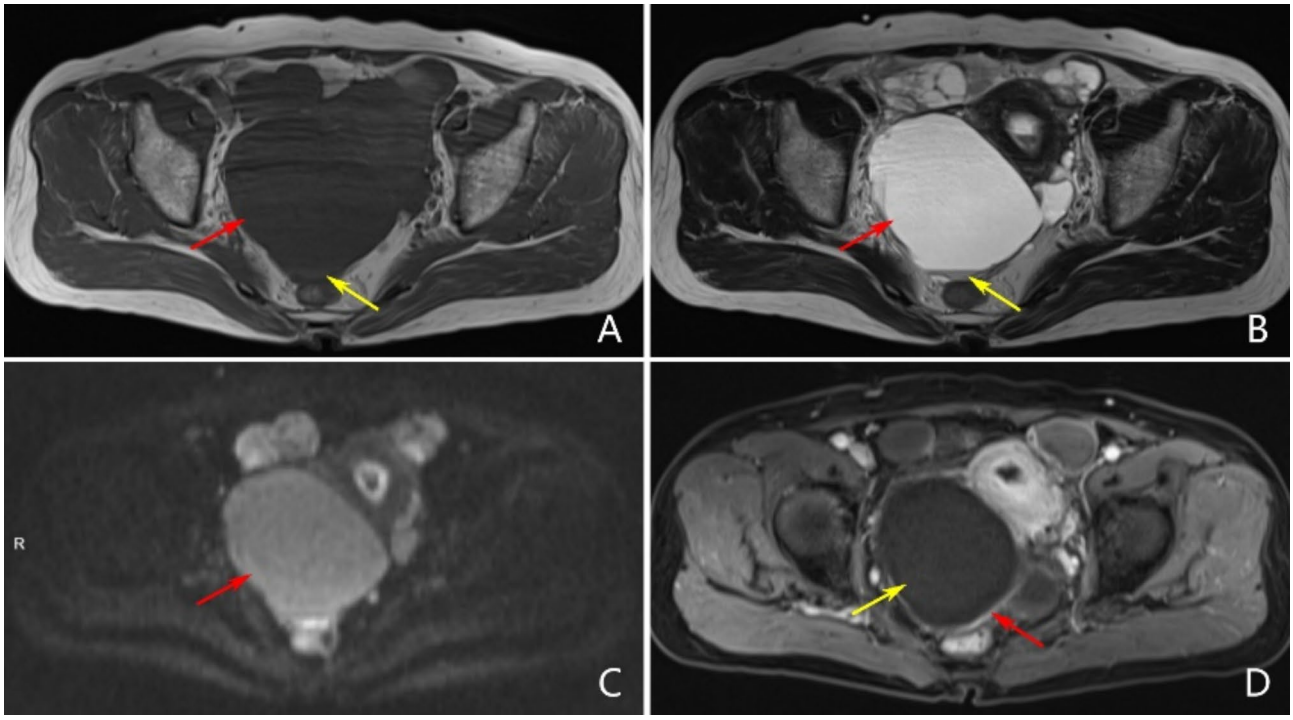

Fig. 1 Patient 9, presented with lower abdominal pain for 5 days, clinically and pathologically confirmed as AGCT-NEL, FIGO stage IIIA. (**A**) T_1WI axial view: A unilocular cystic mass is observed in the right adnexa, well-defined, appearing hypointense on T_1WI (red arrow), with homogeneous signal and the presence of a hemorrhagic fluid level, which appears slightly hyperintense (yellow arrow). (**B**) T_2WI axial view: The mass exhibits very high signal intensity (red arrow), and a hemorrhagic fluid level is visible (yellow arrow). (**C**) DWI sequence: The mass shows slightly elevated signal intensity (red arrow). (**D**) Axial view post-contrast scan: The wall of the mass shows marked enhancement (red arrow), while the contents of the cyst do not exhibit enhancement (yellow arrow)

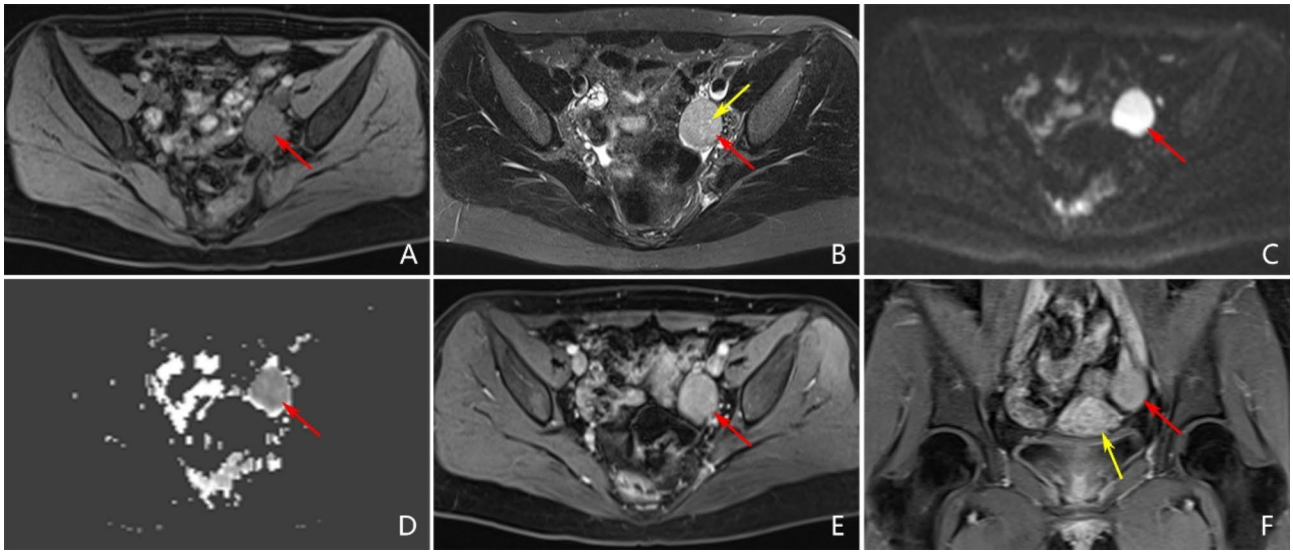

Fig. 2 Patient 7, presented with a left ovarian mass for six months, clinically and pathologically confirmed as AGCT-NEL, FIGO stage IC. (**A**) Axial T_1WI with fat suppression (T_1WI-FS): A solid mass is observed in the left adnexa, well-defined, appearing slightly hypointense on T_1WI (red arrow) with a homogeneous signal. (**B**) Axial T_2WI with fat suppression (T_2WI-FS): The mass shows slightly hyperintense signal (red arrow), with punctate hyperintense foci noted (yellow arrow). (**C**) DWI: The mass demonstrates significantly high signal intensity (red arrow). (**D**) ADCmap: The mass exhibits significantly low signal intensity (red arrow), indicating limited diffusion. (**E**) Axial view post-contrast scan: The mass shows moderate enhancement (red arrow), and the signal remains homogeneous. (**F**) Coronal view post-contrast scan: The mass displays uniform enhancement (red arrow), with enhancement intensity lower than that of the myometrium (yellow arrow)

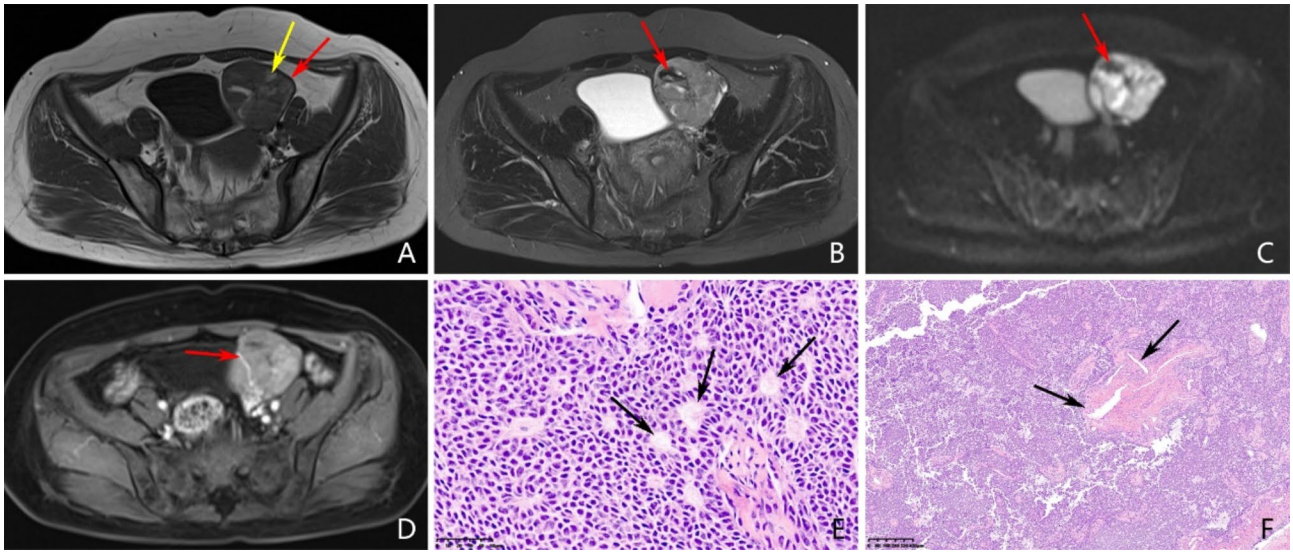

Fig. 3 Patient 2, presented with a pelvic mass for 7 days during a health examination, clinically and pathologically confirmed as AGCT-NEL, FIGO stage IA. (**A**) Axial T_1WI: A cystic-solid mass in the left adnexa is observed (red arrow), predominantly solid, with a intact capsule. The mass appears primarily isointense on T_1WI, with scattered patchy hyperintensities noted (yellow arrow). (**B**) Axial T_2WI-FS: The mass shows predominantly slightly hyperintense signals, while in the areas of high signal observed on T_1WI, T_2WI demonstrates very low signal intensity (red arrow), indicative of hemorrhage. (**C**) DWI: The mass presents significantly high signal intensity, with patchy low signals observed (red arrow), corresponding to the hemorrhage. (**D**) Post-contrast scan: The mass exhibits marked enhancement, with a visible tumor vessel (red arrow). (**E**) Pathology: tumor cells are predominantly round, oval, or polygonal, with some showing lobulation; cells are arranged in clusters or strands, with visible nuclear grooves, intermixed with fibrous tissue components and varying numbers of Call-Exner bodies (black arrow). (**F**) Under 40× magnification: Multiple capillaries are visible (black arrow)

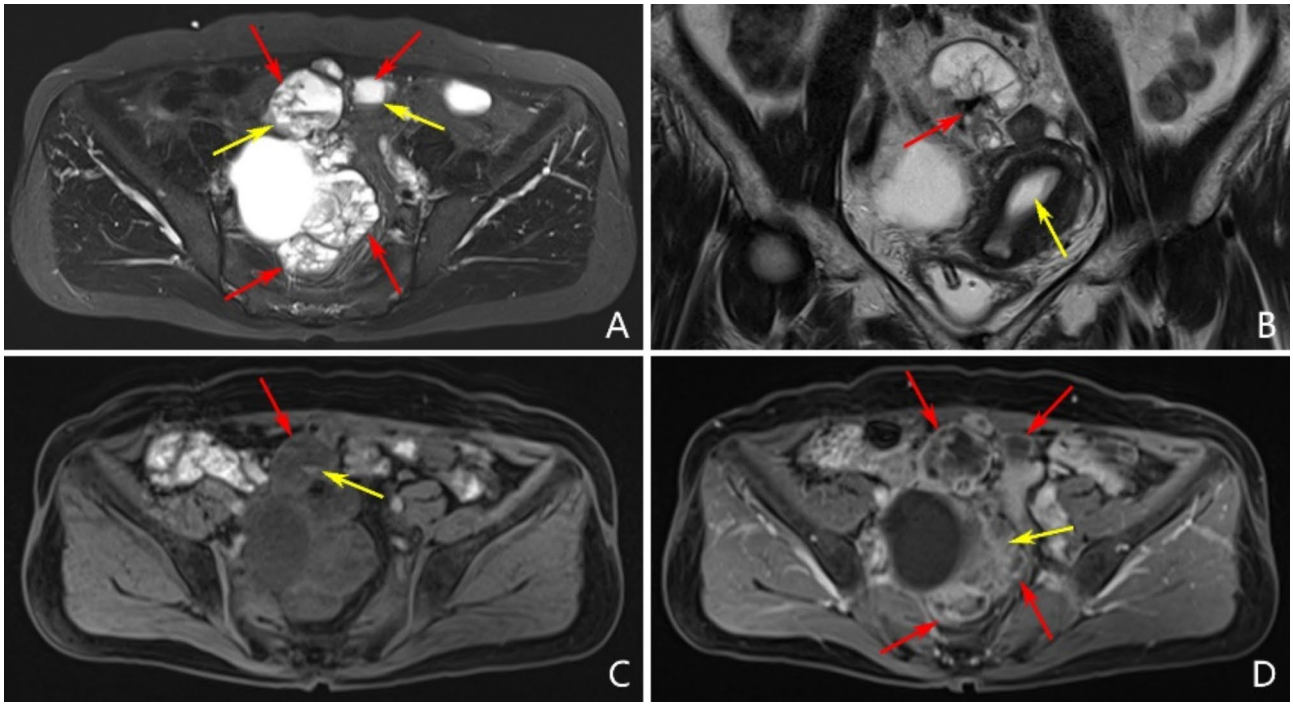

Fig. 4 Patient 9, presented with lower abdominal pain for 5 days, clinically and pathologically confirmed as AGCT-NEL, FIGO stage IIIA. (**A**) Axial T_2WI-FS: Multiple cystic masses are observed in the pelvic cavity, which are either unilocular or multilocular cystic masses (red arrow). The multilocular cystic masses exhibit septations, demonstrating honeycomb and Swiss cheese signs, with hemorrhagic fluid levels visible in several masses (yellow arrow). (**B**) Coronal T_2WI: Punctate very low signal intensity is observed within the multilocular cystic mass (red arrow), indicating hemorrhage. Pathology confirms endometrial thickening (yellow arrow). (**C**) Axial T_1WI-FS: Cystic lesions (red arrow) show scattered hyperintensities (yellow arrow), indicating hemorrhage. (**D**) Post-contrast scan: The cyst wall of the mass (red arrow) and the septations (yellow arrow) exhibit marked enhancement

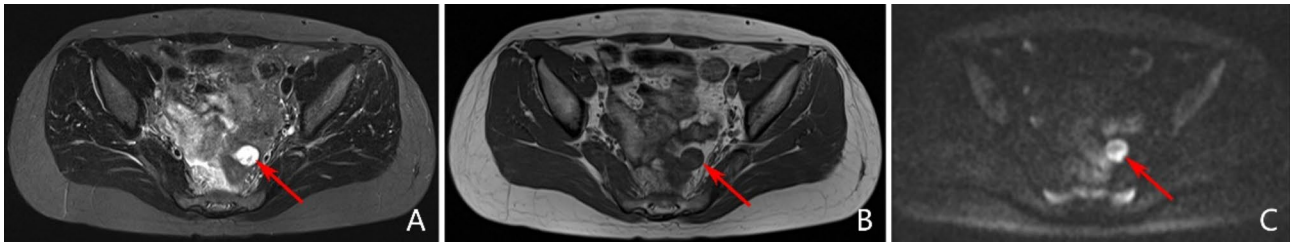

Fig. 5 Patient 10, underwent resection of a primary left adnexal lesion 5 years prior and was found to have a rectal fossa mass (red arrow), clinically and pathologically confirmed as AGCT-NEL, FIGO stage IIIA. (**A**) Axial T_2WI-FS: A multilocular cystic mass in the rectal fossa displays high signal intensity on T_2WI, with visible septations and relatively clear boundaries. (**B**) Axial T_1WI: The mass appears isointense, with relatively clear margins. (**C**) DWI: The mass shows significantly uneven high signal intensity

analysis: all 8 were positive for Vimentin, all 8 were positive for α-inhibin, 7 were positive for CR, and 5 were positive for CD99.

Statistical analysis results

The Kappa values for the analysis of tumor location, number, size, morphology, edge characteristics, signal intensity, and enhancement characteristics by two radiologists were all ≥0.75, indicating good agreement.

Discussion

OGCTs typically have estrogen-secreting functions, and high estrogen concentrations can lead to a range of reproductive system complications [7], such as irregular vaginal bleeding, endometrial hyperplasia, uterine fibroids, and adenomyosis [8–11]. However, approximately 30% of OGCTs exhibit a unique characteristic; due to a lack of theca cells in the tumor stroma, they do not produce estrogen [5]. Therefore, the symptoms and pathological changes observed in the 10 patients with AGCT-NEL in this study (Table 1) cannot be explained by elevated estrogen levels, and the etiology can be quite diverse. For instance, irregular vaginal bleeding could arise from various causes, including inflammation, polyps, or hematological disorders [12]. Certain medications can also induce endometrial hyperplasia [13]. The formation of uterine fibroids is associated with oral contraceptives, smoking, and hormone replacement therapy [14]. Adenomyosis might also stem from developmental abnormalities during the embryonic stage [15]. Even when a mass is noted in the adnexal region, a lack of abnormal elevation in estrogen levels can lead to a misdiagnosis of AGCT. Among the 10 patients in this study, only 1 exhibited a mild elevation in CA-125 (47 U/ml), while the tumor markers for the remaining 9 patients were normal. CA-125 is a classic tumor marker for ovarian cancer [16, 17]. However, based on this study, its auxiliary diagnostic value in AGCT-NEL is limited. This further complicates the diagnostic difficulty and underscores the importance of MRI in diagnosing this disease. In this study, 2 patients had metastases, primarily localized in the pelvis and abdominal cavity, affecting multiple specific sites, which further emphasizes the importance of early diagnosis of AGCT-NEL to minimize the occurrence of metastases. Literature reports indicate that the pelvis and abdominal cavity are the main metastatic sites [18, 19]. however, no pelvic metastases were found in these two cases, which may be related to the inferior diagnostic efficacy of MRI for bone involvement. In the pathological immunohistochemical results, a-Inhibin and Vimentin were positive in 100% (8/8) of cases, CR was positive in 87.5% (7/8), and CD99 was positive in 62.5% (5/8), indicating a distinctive pathological profile [20]. Out of 10 patients, 1 experienced a recurrence 2 years post-surgery, 1 was lost to follow-up, and the other 8 had no recurrence. This low recurrence rate is consistent with the biological characteristics of AGCT-NEL's low malignancy and also indicates that we need to pay sufficient attention to it.

The MRI features of AGCT-NEL primary tumors summarized in this study are as follows: (1) There is a significant variation in tumor size, ranging from approximately 2.9 cm to 21.4 cm (mean 8.1 cm), with the FIGO stage primarily being IA or IC. In contrast, Patient 9 had a maximum diameter of only 8.8 mm for the metastatic primary focus, indicating that the aggressiveness of the tumor and the FIGO stage are not directly related to tumor size. This challenges conventional understanding of tumors and may reflect a biological characteristic of AGCT-NEL. Dridi M et al. also reported similar findings, noting that tumor diameter does not significantly influence the prognosis of OGCT [8]. Additionally, research by Seagle et al. found that among patients with FIGO I stage OGCT, each 1.0 cm increase in tumor diameter corresponded to a 4% increase in mortality risk [21]. Therefore, while diameter does not affect staging, it does contribute to an increased risk of death. (2) Tumor morphology is diverse, primarily presenting as unilocular cystic, solid, or cystic-solid types, which is related to the higher heterogeneity of OGCT compared to other sex-cord stromal tumors [22]. (3) Whether the primary lesion is solid or cystic-solid, the solid component appears isointense or slightly hypointense on T_1WI, exhibits significantly high

signal on DWI, has a notably low ADC value, and shows enhancement lower than the myometrium. Internal features may include hemorrhage or cystic changes. Focal high signals can be seen on T_2WI within the solid mass, possibly indicating early cystic change or microcysts, suggesting that cystic changes could be a characteristic manifestation of the solid component of AGCT-NEL. (4) The cystic portion of the unilocular cystic or cystic-solid primary tumors shows a uniform wall thickness without any nodules, representing a characteristic MRI negative finding for the cystic portion. The cystic part has low signal on T_1WI, very high signal on T_2WI, slightly higher signal on DWI, and an ADC range of approximately 2.567 to 2.940 ($\times 10^{-3}$ s/m^2), and may present with a hemorrhagic fluid level. This indicates that regardless of the type, AGCT-NEL primary tumors may exhibit signs of internal bleeding, with the presence of hemorrhagic fluid level being one of the MRI characteristics of AGCT-NEL [23, 24]. Furthermore, the slightly elevated DWI signal of the cystic fluid corresponds with pathological findings that show a gelatinous texture inside the cyst. (5) The cystic portion of the multilocular cystic tumor may display characteristic honeycomb and Swiss cheese signs.

This study also summarizes the MRI manifestations of metastatic lesions in AGCT-NEL, which are characterized as follows: (1) Implantation and distant metastasis are the primary modes of metastasis for AGCT-NEL, with the metastasis locations primarily concentrated in the pelvic region. (2) All metastatic lesions are cystic (either unilocular or multilocular), and there are no wall nodules present in either type of cystic metastasis, with the internal structure potentially showing hemorrhagic fluid levels. Thus, it can be seen that AGCT-NEL may exhibit signs of bleeding in both primary and metastatic lesions. (3) Multilocular cystic metastatic lesions may display characteristic honeycomb and Swiss cheese signs. (4) In Patient 9, the partitions of the multilocular metastatic lesion is uneven and thickened, which may represent a radiological characteristic of its low malignancy. The primary lesion in Patient 9 is a unilocular cystic mass, while the metastatic mass presents as a multilocular cystic mass, which is rarely reported in the literature regarding post-metastatic features. This may represent one of the characteristic features of OGCT-NEL metastatic lesions.

Currently, research on the MRI features of AGCT-NEL is insufficient. Existing literature generally does not differentiate whether the AGCT secrete estrogen and lacks analysis of the characteristics of metastatic lesions. The findings of this study indicate that the cystic portion of AGCT-NEL has a uniformly thick wall and does not exhibit wall nodules, which have not been reported previously [24, 25]. This study summarizes the MRI features of both primary and metastatic tomurs of AGCT-NEL, providing a more comprehensive overview. Additionally, this research conducted FIGO staging of the lesions and explored some inherent patterns between primary and metastatic lesions and their FIGO stages. However, the study does have certain limitations. Firstly, the sample size for both primary and metastatic lesions is relatively small. As AGCT-NEL is rare, exhibits low malignancy, and typically undergoes surgical resection before metastasis occurs, there is limited data available. Nevertheless, summarizing metastatic lesions holds significant value, particularly for diagnosing postoperative recurrence in patients. Secondly, not all patients underwent enhanced imaging, as most proceeded directly to surgery following routine MRI scans. In the future, we will recommend further enhanced imaging before surgical intervention in similar cases to provide a comprehensive evaluation of the condition and blood supply from an MRI perspective, which can improve diagnostic accuracy and enhance patient safety.

Conclusion

AGCT-NEL is relatively rare and does not produce estrogen, which can easily mislead clinical thinking and result in misdiagnosis. Therefore, accurate MRI diagnosis is crucial. This article analyzes and summarizes the MRI imaging features of AGCT-NEL and identifies some previously unreported imaging manifestations, which holds significant value in enhancing the understanding and diagnostic capability for this condition.

Abbreviations

ADC	Apparent diffusion coefficient
AGCT	Adult granulosa cell tumor
AGCT-NEL	Adult granulosa cell tumor with normal estrogen levels
DWI	Diffusion-weighted imaging
Gd-DTPA	Gadopentetate dimeglumine
MRI	Magnetic resonance imaging
NSA	The number of signal averagesOGCT: Ovarian granulosa cell tumor
SSEPI	Single-shot echo planar imaging
TE	Echo timeTI: Inversion time
TR	Repetition time
TSE	Turbo spin echoT_1WI: T1-weighted imaging
T_1WI-FS	T1-weighted imaging with fat suppression
T_2WI	T2-weighted imaging
T_2WI-FS	T2-weighted imaging with fat suppression
VIBE	The volumetric interpolated breath-hold examination

Acknowledgements

Not applicable.

Author contributions

Wei Weng, Xinle Chi, Yaomeng Chen, Ze Liu and Weiqian Chen wrote the main manuscript text. Jiejie Hu, Huihui Chen, Xindian Pan and Hai Wu prepared figures. All authors reviewed the manuscript.

Funding

None.

Data availability

The data used and analyzed during the current study are available from the corresponding authors on reasonable request.

Declarations

Ethics approval and consent to participate
In accordance with the Declaration of Helsinki, this study was approved by the Medical Ethics Committee of Wenzhou People's Hospital, with informed consent waived.

Consent for publication
Not applicable.

Competing interests
The authors declare no competing interests.

Received: 13 August 2024 / Accepted: 15 December 2024
Published online: 30 December 2024

References

1. Tanaka YO, Tsunoda H, Kitagawa Y, Ueno T, Yoshikawa H, Saida Y. Functioning ovarian tumors: direct and indirect findings at MR imaging. Radiographics. 2004. https://doi.org/10.1148/rg.24si045501.
2. Wu H, Pangas SA, Eldin KW, Patel KR, Hicks J, Dietrich JE, et al. Juvenile Granulosa Cell Tumor of the Ovary: a clinicopathologic study. J Pediatr Adolesc Gynecol. 2017. https://doi.org/10.1016/j.jpag.2016.09.008.
3. Chen VW, Ruiz B, Killeen JL, Coté TR, Wu XC, Correa CN, et al. Pathology and classification of ovarian tumors. Cancer. 2003. https://doi.org/10.1002/cncr.11345.
4. De Giorgi U, Nicolas-Virelizier E, Badoglio M, Bader P, Richard S, Maertens J, et al. High-dose chemotherapy for adult-type ovarian granulosa cell tumors: a retrospective study of the European Society for Blood and marrow transplantation. Int J Gynecol Cancer. 2017. https://doi.org/10.1097/IGC.0000000000000882.
5. Pectasides D, Pectasides E, Psyrri A. Granulosa cell tumor of the ovary. Cancer Treat Rev. 2008.
6. Saida T, Tanaka YO, Matsumoto K, Satoh T, Yoshikawa H, Minami M. Revised FIGO staging system for cancer of the ovary, fallopian tube, and peritoneum: important implications for radiologists. Japanese J Radiol. 2016.
7. Unkila-Kallio A, Tiitinen T, Wahlström P, Lehtovirta A. Leminen. Reproductive features in women developing ovarian granulosa cell tumour at a fertile age. Hum Reprod. 2000. https://doi.org/10.1093/humrep/15.3.589.
8. Stenwig JT, Hazekamp JT, Beecham JB. Granulosa cell tumors of the ovary. A clinicopathological study of 118 cases with long-term follow-up. Gynecol Oncol. 1979. https://doi.org/10.1016/0090-8258(79)90090-8.
9. Van Meurs HS, Bleeker MCG, Van Der Velden J, Overbeek LIH, Kenter GG, Buist MR. The incidence of endometrial hyperplasia and cancer in 1031 patients with a granulosa cell tumor of the ovary: long-term follow-up in a population-based cohort study. Int J Gynecol Cancer. 2013. https://doi.org/10.1097/IGC.0b013e3182a57fb4.
10. Bergeron C, Amant F, Ferenczy A. Pathology and physiopathology of adenomyosis. Best Practice and Research: Clinical Obstetrics and Gynaecology. 2006.
11. Shozu M, Murakami K, Inoue M. Aromatase and Leiomyoma of the Uterus. Seminars in Reproductive Medicine. 2004.
12. Sokol E, Peddinti R. Causes and diagnosis of abnormal vaginal bleeding. Pediatr Ann. 2015;44:e164–7.
13. Montgomtery BE, Daum GS, Dunton CJ. Endometrial hyperplasia: a review. Obstet Gynecol Surv. 2004;59:368–78.
14. Flake GP, Andersen J, Dixon D. Etiology and pathogenesis of uterine leiomyomas: a review. Environ Health Perspect. 2003;111:1037–54.
15. Garcia L, Isaacson K, Adenomyosis. Review of the literature. J Minim Invasive Gynecol. 2011;18:428–37.
16. Aggarwal P, Kehoe S. Serum tumour markers in gynaecological cancers. Maturitas. 2010.
17. Matsas A, Stefanoudakis D, Troupis T, Kontzoglou K, Eleftheriades M, Christopoulos P et al. Tumor markers and their diagnostic significance in Ovarian Cancer. Life. 2023.
18. Abu-Rustum NR, Restivo A, Ivy J, Soslow R, Sabbatini P, Sonoda Y, et al. Retroperitoneal nodal metastasis in primary and recurrent granulosa cell tumors of the ovary. Gynecol Oncol. 2006. https://doi.org/10.1016/j.ygyno.2006.01.050.
19. Dridi M, Chraiet N, Batti R, Ayadi M, Mokrani A, Meddeb K et al. Granulosa Cell Tumor of the Ovary: a retrospective study of 31 cases and a review of the literature. Int J Surg Oncol. 2018.
20. Vang R, Herrmann ME, Tavassoli FA. Comparative immunohistochemical analysis of granulosa and sertoli components in ovarian sex cord-stromal tumors with mixed differentiation: potential implications for derivation of sertoli differentiation in ovarian tumors. Int J Gynecol Pathol. 2004. https://doi.org/10.1097/00004347-200404000-00010.
21. Seagle BLL, Ann P, Butler S, Shahabi S. Ovarian granulosa cell tumor: a National Cancer Database study. Gynecol Oncol. 2017. https://doi.org/10.1016/j.ygyno.2017.05.020.
22. Outwater EK, Wagner BJ, Mannion C, McLarney JK, Kim B. Sex cord-stromal and steroid cell tumors of the ovary. Radiographics. 1998. https://doi.org/10.1148/radiographics.18.6.9821198.
23. Sehouli J, Drescher FS, Mustea A, Elling D, Friedmann W, Kühn W, et al. Granulosa Cell Tumor of the Ovary: 10 years follow-up data of 65 patients. Anticancer Res. 2004;24(2):1223–9.
24. Morikawa K, Hatabu H, Togashi K, Kataoka ML, Mori T, Konishi J. Granulosa cell tumor of the ovary: MR findings. J Comput Assist Tomogr. 1997. https://doi.org/10.1097/00004728-199711000-00028.
25. Zhang H, Zhang H, Gu S, Zhang Y, Liu X, Zhang G. MR findings of primary ovarian granulosa cell tumor with focus on the differentiation with other ovarian sex cord-stromal tumors. J Ovarian Res. 2018. https://doi.org/10.1186/s13048-018-0416-x.

Publisher's note